Review

Important Technical Considerations in Design of Battery Chargers of Electric Vehicles

Mahdi Bayati [1], **Mehrdad Abedi** [1], **Maryam Farahmandrad** [2], **Gevork B. Gharehpetian** [1] **and Kambiz Tehrani** [3,*]

1   Department of Electrical Engineering, Amirkabir University of Technology, Tehran 15875-4413, Iran; bayati.mahdi@aut.ac.ir (M.B.); abedi@aut.ac.ir (M.A.); grptian@aut.ac.ir (G.B.G.)
2   Bu-Ali Sina University, Shahid Mostafa Ahmadi Roshan Street, Hamedan 6516738695, Iran; m.farahmandrad@alumni.basu.ac.ir
3   ESIGELEC-IRSEEM, Normandy University, 1002476801 Rouen, France
*   Correspondence: tehrani@esigelec.fr or kambiz.tehrani@ieee.org

Abstract: There are many important trade-offs and constraints on cost, volume, weight, conduction losses, switching losses, microcontrollers, isolation, voltage and current levels, voltage and current ripples, battery specifications, charging–discharging algorithms, control system, switch gate drivers, and efficiency of battery chargers in electric vehicles. In this paper, a well-known power electronic topology commonly used in recent relevant studies is considered, and some important technical considerations with regard to the mentioned trade-offs and constraints are discussed in detail for the first time. The discussion concerns the practical and theoretical experiences in implementation of battery chargers and charging stations of electric vehicles exclusively, and it can be extended to various other power electronic topologies.

Keywords: battery charger; charging station; converter; electric vehicle

1. Introduction

Nowadays, the design of charging stations and battery chargers of electric vehicles (EVs) is being extensively studied. In this paper, a well-known topology for battery chargers and charging stations of EVs was selected, and then personal experiences in some particular aspects of power electronics in the design of EV battery charging systems were explained in detail. The purpose of this paper is to explain challenges and technical considerations in the projects published in [1–6]. In [1], a special parallel capacitor battery structure for an EV charging system founded on a pulse-current charging–discharging method with its control system has been put forward to exchange constant continuous power in front of drastic changes in the battery power. In [2], two DC-DC converters with their control systems have been proposed for EV charging systems. They impose pulse-current and pulse-voltage charging methods on the battery pack. In [3], an EV battery charger was introduced, and then a control system was exactly designed in order to create a sinusoidal-ripple-current (SRC) charging–discharging technique and to control the output active and reactive powers during vehicle-to-grid technology. In [4,5], an EV battery charger was introduced such that it can help a power system and participate in vehicle-to-grid technology. The designs of all EV charging systems in [1–6] have many areas that can be carefully examined, such as cost, volume, weight, conduction losses, switching losses, microcontrollers, isolation, voltage and current levels, voltage and current ripples, battery specifications, charging–discharging algorithms, control system, switch gate drivers, and efficiency of battery chargers of EVs. In this paper, these areas are spelled out. The discussions are very worthwhile because the topology is very common, the subjects are exclusive to EVs and can be extended to various topologies, and it will definitely help engineers to carefully and cleverly design EV battery

chargers. The topology studied in this paper is similar to the topologies implemented in [1–6], as well as in [7–43].

In keeping with the topologies in [1–43], Figures 1 and 2 show the three-phase and single-phase power electronic topologies for which its technical considerations are supposed to be examined. This paper focuses on the three-phase type. This three-phase type includes two parts: DC-DC and DC-AC stages. Such a structure can be seen in a lot of papers such as [1–5,8,18,44–48]. The DC-AC part is a three-phase two-level voltage source converter, and the DC-DC part is one non-isolated half-bridge DC-DC converter, which is named the IGBT leg. The IGBT leg $Q_7 Q_8$ is very well-known in power electronics and is commonly used in many applications such as wind turbines and solar panel interfaces, as well as in EV battery chargers and charging stations [1–42]. In [7,40], an IGBT leg is mathematically modelled; it explains how to connect these elements to make various topologies. In [8], the effects and stability of an IGBT leg in a DC distribution system are studied. In [9–12,28], some parallel IGBT legs are controlled to share a constant power between some batteries. In [13], an IGBT leg is utilized for electrochemical impedance spectroscopy (EIS) of batteries. In [14–16,41], an IGBT leg is used in hybrid energy storage systems for EVs. In [17], some IGBT legs are connected in an EV charging station in order to enable it to participate in vehicle-to-grid technology. In [18,21], the limitations on the combination of IGBT legs to generate active and reactive power are examined. In [19,20], an IGBT leg is employed to impose pulse-current charging–discharging algorithm on an EV battery. In [22,24,29,30,32,34,35,39], an EV battery charger with a combination of IGBT legs is designed. In [23], an IGBT leg, as a building block, is utilized in various kinds of power electronic converters embedded in the EV. In [25,31–33], a neutral point clamped converter is made of some IGBT legs for an EV charging station. In [26,36–38,42], a power electronic interface for an EV including a battery pack and an ultracapacitor is designed by combining some IGBT legs in DC-AC and DC-DC parts. In [27], IGBT legs with a battery pack and an ultracapacitor form a battery-ultracapacitor storage system. In [43], an EV battery charger with three IGBT legs is proposed to work on different modes in vehicle-to-grid technology. Consequently, this topology is worthy of study because it has similar components and is very similar to thousands of non-isolated converters extensively used and developed for battery chargers.
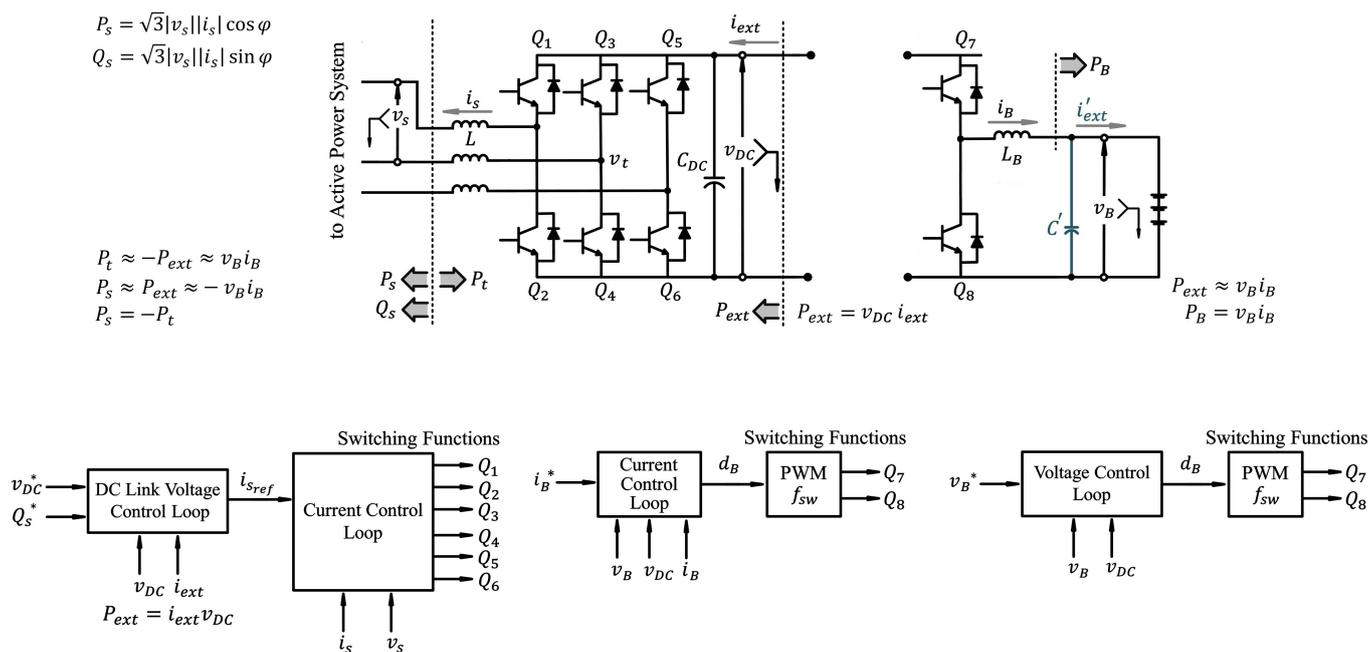

Figure 1. Common three-phase configuration for EV battery chargers with its control system.
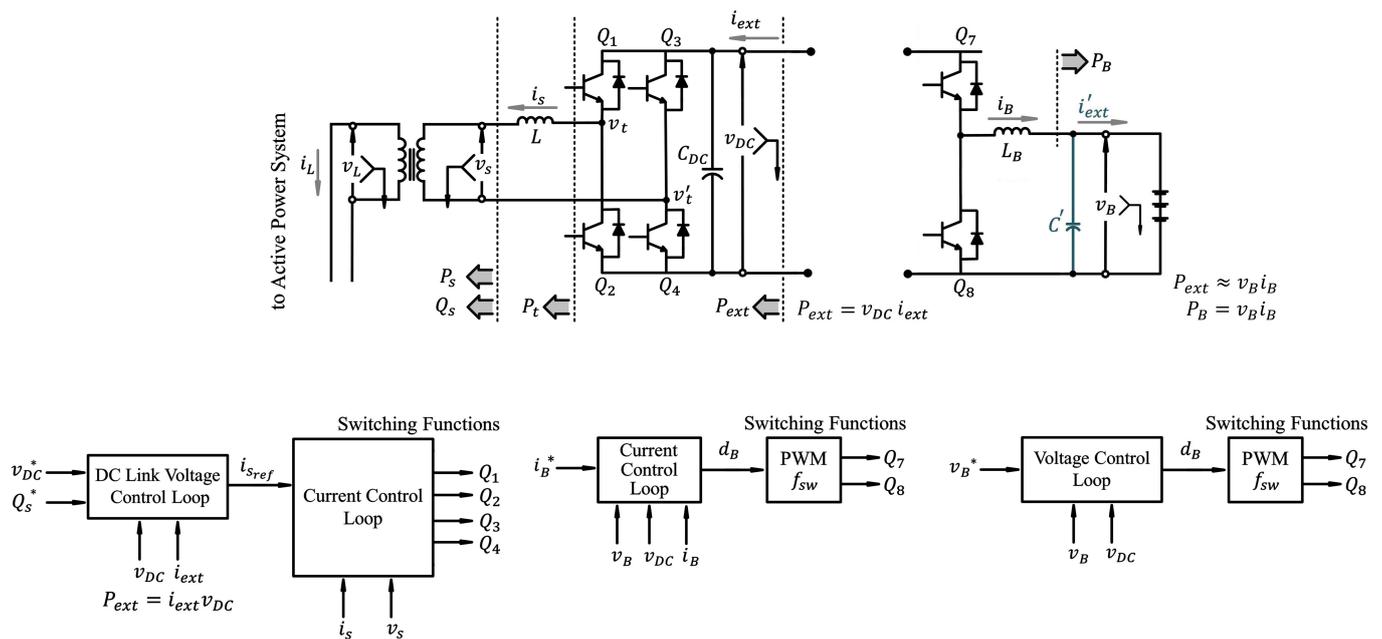
Figure 2. Common single-phase configuration for EV battery chargers with its control system.

The purpose of this research study is to discuss the challenges and technical considerations in the projects published in [1–6]. Moreover, the original contribution of this paper is to theoretically and practically justify the challenges and technical considerations that are related to the most important building blocks of EV battery chargers, that is, the IGBT leg. This study explains how elements, voltage levels, current levels, and other components must be selected based on theoretical and practical reasons and not by accident. It will uniquely address these issues in detail in comparison to the recently published papers in the field of EV battery chargers based on practical experiences and theoretical justifications. For instance, the selection of an appropriate microcontroller, selection of the appropriate inductance, selection of the switching and charging frequencies, and the selection of the reference command of the DC link voltage to reduce the switching dissipation and to maximize the output reactive power and so on are vindicated in this paper in practice and in theory for an EV battery charger including some IGBT legs.

2. General Overview

Figures 1 and 2 also show the general overview of their control systems. In general, the DC-DC stage controls the battery voltage v_B or the battery current i_B, and the DC-AC stage regulates the DC link voltage v_{DC} along with the output reactive power Q_s. These control objectives are achieved by switching on and off the switches Q_1 to Q_8 as the outputs of the control systems. The control systems in Figures 1 and 2 and their detailed descriptions in Figures 3 and 4 are explained more in the next sections. They have also been explained in detail in [1–7,45].
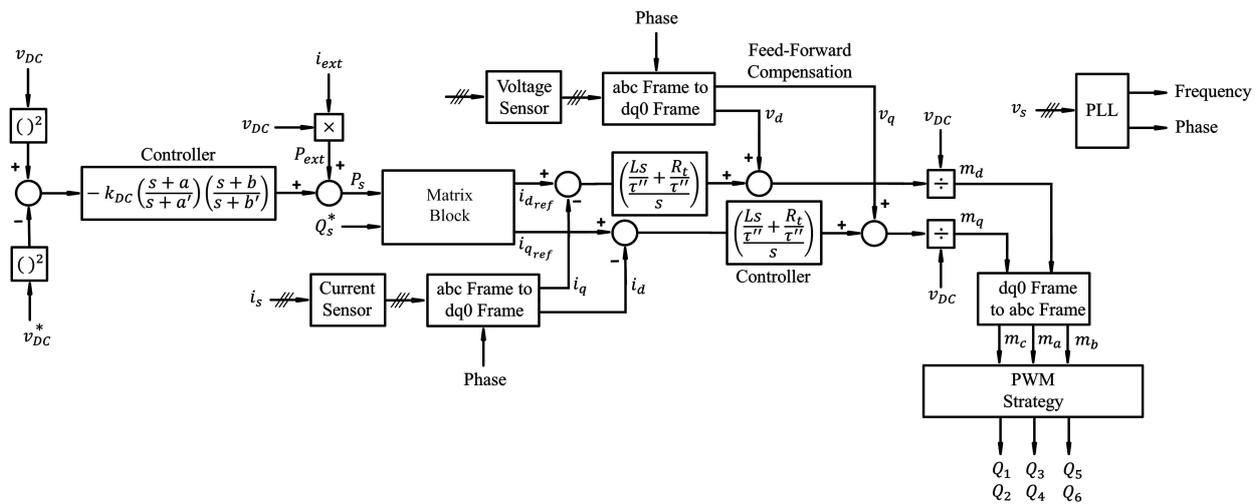
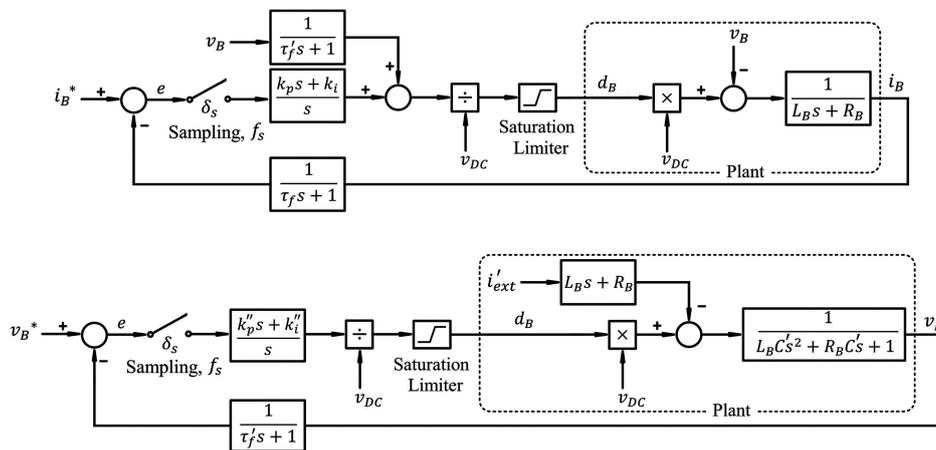**Figure 3.** Detailed description of the control block diagrams of the DC-AC part depicted in Figure 1.

Figure 4. Detailed description of the control block diagrams of the DC-DC part depicted in Figures 1 and 2.

3. Trade-Offs and Constraints

3.1. Switching and Conduction Losses

Each power electronic system has two types of losses: switching and conduction. The power electronic topology shown in Figure 1 is composed of four similar IGBT legs (bidirectional two-level half-bridge voltage source converters) in a particular way. One of them has been separately illustrated on the left side of Figure 5. In reality, it is not ideal. Thus, the non-ideal characteristic of the leg Q_iQ_{i+1} on the left side of Figure 5 is worthy of discussion.

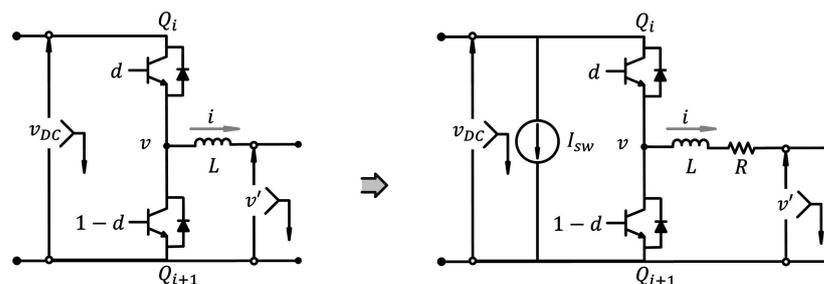

Figure 5. Conduction and switching losses of a non-ideal IGBT leg.

In [7], the pulse-width modulation (PWM) switching strategy for an IGBT leg has been thoroughly examined. The averaged value of the voltage at the middle of the leg, v,

in the non-ideal half-bridge two-level voltage source converter in Figure 5 is given by the following [7]:

$$v(t) = d(t)v_{DC} - \frac{i(t)}{\mid i(t) \mid}v_e - r_e i(t) \tag{1}$$

where v_e and r_e are defined by

$$v_e = v_d - \left(\frac{Q_{rr} + Q_{tc}}{T_{sw}}\right)r_{on} + v_{DC}\left(\frac{t_{rr}}{T_{sw}}\right), \tag{2}$$

$$r_e = \left(1 - \frac{t_{rr}}{T_{sw}}\right)r_{on} \approx r_{on}. \tag{3}$$

The letter t in the parentheses indicates that the corresponding variable is a signal, a function of time, and can change as time passes. For instance, $d(t)$ means that d is a function of time and the control system changes d to make the desired condition. t_{rr}, t_{tc}, and r_{on} are the reverse recovery time, the tailing time, and the on-state resistance of one IGBT, respectively. These parameters are related to the characteristics of the two IGBTs in the leg Q_iQ_{i+1}. Q_{rr}, Q_{tc}, and T_{sw} are the reverse recovery electric charge of one IGBT, the tailing electric charge of one IGBT, and the switching period, respectively. Q_{rr} and Q_{tc} are also related to characteristics of the two IGBTs in the leg Q_iQ_{i+1}. $i(t)$, v_{DC}, and $d(t)$ are the current flowing through the inductor connected to the leg Q_iQ_{i+1}, the DC link voltage, and duty cycle of the upper switch Q_i, respectively. v is controlled based on (1). The first term on the right side of Equation (1), dv_{DC}, represents a dependent voltage source that can be regulated by the duty cycle signal. The third term, $r_e i$, can be regarded as an ohmic voltage drop. The second term, $i/ \mid i \mid v_e$, represents a voltage offset for which its polarity is dependent on the polarity of the current flowing through the inductor L. If i is negative, the voltage offset is added, whereas the voltage offset will be subtracted if it is positive.

As Equation (1) suggests, the second term introduces a dead zone in the control characteristic function from d to v, associated with the current zero crossing. Consequently, v is slightly distorted compared to a pure waveform of d. The distortion is negligible since v_e is typically only a fraction of one volt. This value is significantly smaller than the typical voltage levels for converters in EV battery chargers [7]. The impact of the distortion is further mitigated since d is often controlled by a closed-loop control scheme that attempts to force i to track a distortion-free reference command. For these reasons, we no longer tackle the voltage distortion issue in the subsequent formulations and approximate Equation (1) by the following [7].

$$v \approx dv_{DC} - r_e i \approx dv_{DC} - r_{on} i. \tag{4}$$

As discussed in [7], the averaged model of the non-ideal bidirectional two-level half-bridge voltage source converter can be constructed by augmenting the averaged model of an ideal counterpart with two parasitic components:

- The resistance of the IGBT during "on state" (r_{on}) linked in series to the internal resistance of the inductor. The resultant resistance is named R, as shown in Figure 5. R equals r_{on} plus the internal resistance of the inductor L.
- An independent current source linked in parallel to the capacitor of the DC bus, C_{DC}. It is named I_{sw}, as shown in Figure 5.

The former predominantly pertains to the conduction dissipation, and the latter mainly pertains to the switching dissipation. As illustrated in Figure 5, the non-ideal average model can be treated as the ideal average model together with one resistance in addition to L, named R, and an equivalent independent current source linked in parallel to v_{DC}, named I_{sw}, which is equal to the following [7].

$$I_{sw} = \frac{\left(Q_{rr} + Q_{tc}\right)}{T_{sw}}. \tag{5}$$

Since r_{on} and I_{sw} are approximately constant and independent of the voltages and currents, they can be lumped with the both sides, v' and v_{DC}, respectively. Now, the switching losses and the conduction losses for the single IGBT leg in Figure 5 can be expressed as follows [7].

$$P_{sw} = v_{DC} \times I_{sw}, \tag{6}$$

$$P_{con} = R \times i(t). \tag{7}$$

Obviously, P_{sw} and P_{con} can be separately evaluated for each four IGBT legs in the proposed power electronic structure shown in Figure 1. If we combine (5) with (6), a better description for the switching losses is reached.

$$P_{sw} = v_{DC} \times I_{sw} = v_{DC} \times \frac{\left(Q_{rr} + Q_{tc}\right)}{T_{sw}} = v_{DC}\left(Q_{rr} + Q_{tc}\right)f_{sw}. \tag{8}$$

This value pertains to a single IGBT leg. The switching losses for the proposed system in Figure 1 is exactly four times greater than this value as stated in (9) and (10) because there are four IGBT legs.

3.2. Efficiency

The power flowing through a branch equals the product of the instantaneous current and voltage of the branch. Therefore, it can be extended to all the branches in the power electronic topology shown in Figure 1 (see the equations written in Figure 1). Therefore, the efficiency of the EV battery charger can be calculated in the charging mode as follows.

$$E = \frac{P_B}{P_t} = \frac{P_t - \sum_{i=1}^{i=4} P_{con}^i - \sum_{i=1}^{i=4} P_{sw}^i}{P_t} = \frac{P_t - \sum_{i=1}^{i=4} P_{con}^i - 4P_{sw}}{P_t} = \frac{P_t - \sum_{i=1}^{i=4} P_{con}^i - 4I_{sw}v_{DC}}{P_t} \tag{9}$$

It can be calculated in the discharging mode as follows.

$$E = \frac{P_t}{P_B} = \frac{P_B - \sum_{i=1}^{i=4} P_{con}^i - \sum_{i=1}^{i=4} P_{sw}^i}{P_B} = \frac{P_B - \sum_{i=1}^{i=4} P_{con}^i - 4P_{sw}}{P_B} = \frac{P_B - \sum_{i=1}^{i=4} P_{con}^i - 4I_{sw}v_{DC}}{P_B} \tag{10}$$

The switching dissipation and conduction dissipation create a difference between the input power and the output power. The input power equals P_t, and the output power equals P_B during charging; conversely, the input power equals P_B, and the output power equals P_t during discharging. The power difference determines the efficiency. More switching and conduction losses cause less efficiency. All four IGBT legs have the conduction and switching losses. Each IGBT leg has its own switching and conduction losses that have been formulated in (6) and (7). P_{sw}^i is regarded as the switching dissipation in leg i, and P_{con}^i is regarded as the conduction dissipation in leg i. Since P_{sw}^i relies heavily on the properties of the switches and the switching frequency f_{sw} according to (5) and (6), it has the same value for all the four IGBT legs in the configuration depicted in Figure 1. This idea has been employed in (9) and (10).

Now, the general equation of power in the EV battery charger can be expressed as follows.

$$P_s \approx P_{ext} \approx -P_B = -i_B v_B. \tag{11}$$

Assume that the control system in the DC-AC part successfully works, it is in steady-state condition, and v_{DC} tracks v_{DC}^*. Considering the stability of v_{DC} and the fact that the variable v_{DC} becomes equal to the constant reference command v_{DC}^*, we can say that the following is in a steady-state condition.

$$\frac{d}{dt} v_{DC} = 0 \tag{12}$$

Equation (12) means that the current flowing through C_{DC} must be mathematically zero because the following is the case.

$$i_{C_{DC}} = C_{DC} \frac{d}{dt} v_{DC} = 0. \tag{13}$$

In other words, C_{DC} works similar to a bridge, which allows the power to cross over it. In conclusion, the power in the DC-DC part is transferred to the DC-AC part and in reverse because the DC link takes in no current. If the conduction and switching losses are neglected, the power in the DC-DC stage has exactly the same value in the DC-AC part. Contrarily, this power is not completely transferred from the DC-DC part to the DC-AC part and in reverse, and approximate equality for expressing the power equations must be used. For the DC-DC part, we have the following.

$$- P_{ext} \approx v_B i_B \tag{14}$$

For the DC-AC part, we have the following.

$$P_t \approx -P_{ext} \tag{15}$$

Since $P_s = -P_t$, Equation (14) can be combined with Equation (15).

$$P_s \approx -v_B i_B. \tag{16}$$

Accordingly, the following constraints and trade-offs can be inferred:

- Obviously, high-quality electrical elements with low resistances, for instance, IGBTs with little r_{on} and inductors with little internal resistances can be used in order to decrease the conduction losses according to (7), (9), and (10). On the other hand, using high-quality elements increases cost because they are more expensive.
- Lower v_{DC}, IGBTs with lower Q_{rr} and Q_{tc}, and lower switching frequency f_{sw} can be selected in order to decrease the switching losses according to (6), (9), and (10). On the other hand, the following is also the case:
  - Lower v_{DC} decreases cost because the capacitor C_{DC} with lower nominal voltage is used. Capacitors with lower nominal voltages are cheaper.
  - Lower v_{DC} reduces the maximum ability of the IGBT leg to inject current to the battery. The maximum possible value for the battery current is decreased (see Section 3.9). In fact, the high-side voltage (v_{DC}) has less power to inject the energy to the battery.
  - Lower v_{DC} increases the duty cycle of the IGBT leg (d_B), and the control system proceeds towards the saturation condition. The duty cycle is limited to zero and one. Lower v_{DC} results in duty cycles close to one (near saturation condition or over-modulation [7]).
  - IGBTs with lower Q_{rr} and Q_{tc} increase cost because more expensive switches are bought.
  - Lower switching frequency f_{sw} involves slower switches, thereby decreasing cost. Switches with lower speeds are cheaper.
  - Lower switching frequency f_{sw} causes an increase in the amplitude of the ripple of the battery current i_B. The inductance of the IGBT leg (L_B) should be selected higher in order to decrease the ripple. However, it increases cost, volume, and weight.
- According to (9) and (10), a decrease in the conduction losses and the switching losses obviously means an increase in the efficiency.
- The switching loss P_{sw} depends heavily on the characteristics of the IGBTs (Q_{rr} and Q_{tc}), the switching frequency (f_{sw}), and the DC link voltage (v_{DC}). In order to decrease P_{sw} due to an increase in v_{DC}, higher-quality IGBTs with higher voltage and power levels can be utilized. These values heavily depend on the characteristics of the IGBTs, design of the IGBT gate drivers, and so on. On the other hand, P_{sw} is

commonly assessed as the percentage of P_{in} or P_{out}. It is sensible to compare P_{sw} with P_{in} and P_{out} for each prototype. In fact, the efficiency can be an index for making reasonable assessments.

3.3. Transformer and Isolation

Battery chargers are divided into two groups, non-isolated and isolated. The isolation refers to the existence of an electrical barrier between the input and the output of the battery charger. An isolated converter in the battery charger usually uses a transformer to eliminate the path between its input and output. In contrast, a non-isolated converter does not have such a path. For safety considerations, the isolation must be considered. The isolation in non-isolated converters is a little more complicated. Figure 1 without the transformer shows a non-isolated configuration. In spite of the isolation problem, it has many great advantages such as simplicity in design, less number of elements, low cost, high power density as against the isolated one.

In spite of the fact that galvanic isolation negatively affects efficiency, power density, and cost [49], on-board battery chargers are made up of an isolated converter with a transformer in their design. Standards for safety of EVs such as SAE J1772 [49,50] clearly state that galvanic isolation is not necessary. In addition, the battery pack can be isolated from the AC-side terminal due to the fact that the ground generally floats with the ground of the EV [49,50]. Moreover, other power electronic converters for the battery pack can enter the "off state" when the EV battery charger is working [49]. By way of safety, a relay can be connected to the output or an isolation monitoring mechanism can be utilized to have the same roles of transformers in isolated structures [46,49,51,52]. Hence, a high-power, high-efficiency, low-cost, and non-isolated battery charger is reasonable. This type of on-board battery charger features strong points of decreasing losses, cost, weight, and volume because the transformer can be eliminated. Moreover, in off-board applications and charging stations, a line-frequency transformer (as shown in Figure 1) can be added. It can isolate the battery from the microgrid.

Adding a transformer has advantages and disadvantages. It can be effective for the following reasons:

- It creates isolation.
- With the exception of isolation, the transformer has a duty to provide reduced voltage for the converter. It considerably increases the reactive power generation and causes the control system to work far from the saturation condition. Overmodulation occurs when the control system in the DC-AC part generates the duty-cycle control signals for the IGBTs more than one. The over-modulation entails low-harmonics in the spectrum of the AC-side terminal current and voltage [7]. Moreover, the control system cannot successfully track the reference commands of P_s and Q_s (P_s^* and Q_s^*, respectively), and the power quality thereby deteriorates. In order to avoid the over-modulation, the magnitude of the AC-side terminal voltage of the voltage source converter has to be kept at less than half of the magnitude of v_{DC} [7]. We have the following.

$$\frac{v_{DC}}{2} \geq \hat{v}_t. \tag{17}$$

According to [7], Equation (17) is differently stated as follows.

$$\frac{v_{DC}}{2} \geq \left\{ \hat{v}_s^2 + \frac{4}{9}\left(\frac{L\omega_0}{\hat{v}_s}\right)^2\left(P_s^2 + Q_s^2\right) + \frac{4L\omega_0}{3}Q_s + \frac{4}{9}\left(\frac{L\omega_0}{\hat{v}_s}\right)^2\left(\left(\frac{1}{\omega_0}\frac{d}{dt}P_s\right)^2 + \left(\frac{1}{\omega_0}\frac{d}{dt}Q_s\right)^2\right) \right.$$
$$\left. + \left(\frac{4L\omega_0}{3} + \frac{8}{9}\frac{L\omega_0}{\hat{v}_s}^2 Q_s\right)\left(\frac{1}{\omega_0}\frac{d}{dt}P_s\right) + \left(\frac{-8}{9}\frac{L\omega_0}{\hat{v}_s}^2 P_s\right)\left(\frac{1}{\omega_0}\right) \right\}^{0.5}. \tag{18}$$

lIt includes steady-state and transient parts. The derivative parts are approximately zero during steady-state conditions. Thus, Equation (18) can be written even smaller. By assuming $L\omega_0 \ll v_s$, Equation (18) is rewritten as follows [7].

$$\frac{v_{DC}}{2} \geq \sqrt{\hat{v}_s^2 + \frac{4L\omega_0}{3}Q_s + \frac{4L}{3}\frac{d}{dt}P_s}. \tag{19}$$

Thus, there are typically serious technical limitations on Q_s and the rate of change of P_s; that is, dP_s/dt. The reference command of Q_s must be confined in order to avoid the overmodulation when the system works under steady-state condition. Rate limiters and saturation limiters have been used and adjusted for the control system based on the maximum values of Q_s and dP_s/dt. The control system cannot appropriately work without help of these limiters. Based on Equation (19), it is inferred that Q_s increases for a specific value of v_{DC} if v_s is decreased. Therefore, if the transformer creates the voltage difference between the microgrid and the converter (that is, it reduces v_s), the ability of the converter in reactive power generation is greatly enhanced.

Equation (19) also reveals that we can use lower v_{DC} if v_s decreased. This means that we can purchase a cheaper DC link capacitor (C_{DC}) with lower nominal voltage. Additionally, if v_{DC} is decreased, the switching losses decrease according to the mentioned discussions about the switching losses. On the other hand, lower v_{DC} reduces the maximum ability of the IGBT leg to inject current to the battery and to push the control system towards the saturation condition.

If the voltage level at the AC-side terminal v_s is reduced, the current level increases for a specific constant power level. This means that more current flows through the inductor L and the transformer (shown in Figure 1); thus, the conduction losses increase. Increases in volume, weight, and cost are other disadvantages of the three-phase transformer.

3.4. Battery Current Ripple

Selecting appropriate levels has many challenges and trade-offs. Switching and conduction losses are important criteria for designs, but they are not the only one. All criteria must be considered. To have a better view of this, the ripple of the battery current i_B is considered as another criterion for the design [53,54]. These ripples have been shown in Figure 6. Minimizing the ripple is an important common criterion for the design of a battery charger based on power electronic topologies [53,55]. The amplitude of the battery current ripple should be less than 10% according to the standards. It becomes smaller because of the following:

- There is an Increase in the inductance of the leg Q_7, Q_8, and L_B.
  If L_B is raised, cost, weight, and volume are correspondingly raised.
- A drop in the upper voltage of the legs, v_{DC}, occurs:

  - If v_{DC} is reduced, the switching losses decrease according to (8).
  - Since the elements such as the capacitors and the switches with lower voltage constraints are bought, the cost is cut.
  - The control system approximates to the saturation situation, which is when the duty cycle exceeds one or rather the modulating signal exceeds one and minus one. Simply put, v_{DC} is not powerful enough to make the reference currents when it becomes more than one. The maximum possible current injected to the battery pack is restricted by (v_{DC}) and the sum of (r_{on}) and (R) and the sum of the resistances in the path of each leg. The drop in v_{DC} is not desired because it is bound to operate under the saturation condition.
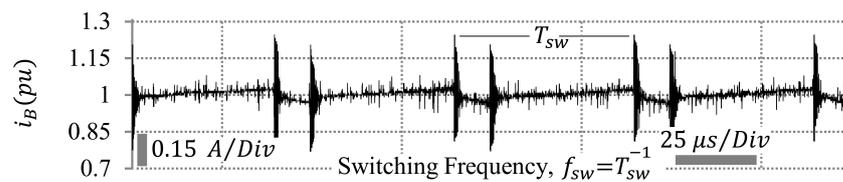
Figure 6. Ripple of the battery current i_B.

- A rise in the switching frequency, f_{sw}, occurs:
    - The more f_{sw} the system works with, the more switching dissipation it possesses.
    - Faster IGBTs are used, thus increasing the cost. Moreover, f_{sw} must be greater (at least ten times) than the charging frequency f_c in order to have a recognizable waveform for the battery current.
    - f_{sw} must be at least 10 times greater than the bandwidths of the control loops (see the control loops in [2,3]).
    - f_{sw} cannot increase a lot because the bandwidths of the current and voltage sensors must be enhanced again. On the other hand, the sampling frequency of the microcontroller f_s shown in Figure 4 and the clock frequency of the microcontroller must be also enhanced.

It is necessary to make the battery current ripple less. The current levels, the voltage levels, and the parameters are adjusted such that volume, weight, cost, conduction losses, and switching losses are optimized.

3.5. Voltage Stress

There are two types of voltage stress that occur across a semiconductor device:

- The first type occurs during the transition periods, from the on state to off state and vice versa. Power electronic switches are used to open and close a circuit. When a circuit is opened, the current flowing through it is interrupted. The change in the current during a short period of time (di/dt) will be very big. It causes the switch to melt. During conduction, when the switch is closed, the voltage difference across two terminals will be ideally zero. However, when the circuit is open, a high voltage difference develops across the switch (dv/dt). This also causes damage to the switch and ultimately the whole topology. In order to overcome this problem, a switch that has less turn-off time, uses snubber circuits, and has betterdesigned gate drivers is required.
- The second type occurs when it is reverse biased or in an off state. To overcome such a voltage stress, a switch that has a higher breakdown voltage with a safety margin is needed. The voltage stress also depends upon the type of converter one is using. In the case of the topology in this paper, the IGBTs will always be stressed to v_{DC}. Alternative DC-AC topologies such as multi-level ones can be used to reduce the stress across each IGBT. Moreover, v_{DC} can be decreased. Although a decrease in v_{DC} results in a decrease in the switching losses and voltage stress, it causes saturation in the control loops and limits the maximum current delivered to the battery pack

3.6. Switch Gate Drivers

The switch gate drivers are divided into two main categories: the ones that isolate the control part from the power part and the ones that do not provide this isolation. In sensitive cases, each IGBT gate driver must provide isolation between the control part and the power part. The optocoupler gate drivers are the ones which provide isolation based on an optic isolation method [56]. Figure 7 shows the typical electrical circuit of the IGBT optocoupler gate driver, HCPL315J. This electrical circuit pertains to a single IGBT leg and consists of two parts, the control part and the power part. The switching functions are the inputs. They are time-varying and digital. The buffer SN74LS07 receives

them, and then it amplifies them. This buffer prevents the microcontroller from breaking down because the pins of the microcontrollers cannot usually tolerate the currents more than 4 mA. The buffer should also be faster than the optocoupler gate driver integrated circuit (IC) and the microcontroller in that it can easily follow the reference commands. The optocoupler IGBT gate driver is able to receive the switching functions and separately generate gate-emitter voltages for each IGBT. The resistances in the output and the input, the amplitude of the floating voltage supply, and the capacitances are the parameters in the recommended circuit for HCPL315J that must be calculated based on the characteristics in the datasheet of the IGBT. Therefore, we must redesign it whenever the IGBT is replaced with a different one. In fact, the new IGBTs have different nominal values and characteristic curves; thus, this circuit must be inevitably redesigned.
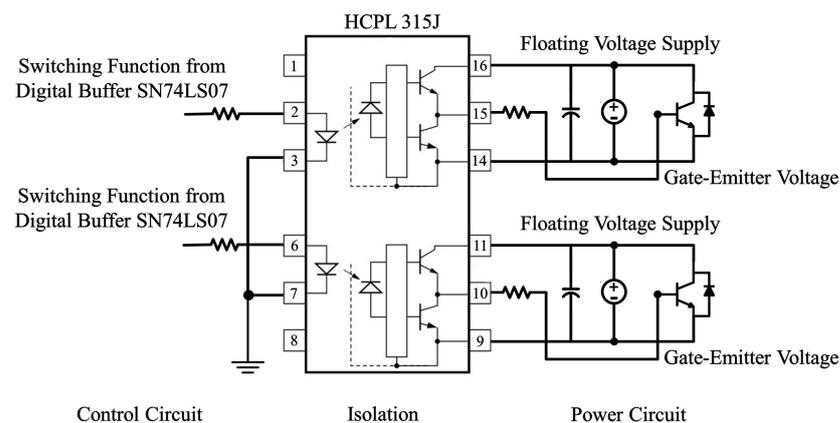

Figure 7. Typical electrical circuit as the IGBT optocoupler gate driver.

The circuit is worthy of mention because each optocoupler gate driver IC must be able to implement the switching frequency f_{sw}. Thus, in addition to the characteristics of the switches, the switching frequency f_{sw} affects the selection of the optocoupler gate driver ICs. The resolution is also important. For instance, some optocoupler gate drivers are able to impose the turn-on and turn-off signals on the switches with the frequency of 200 kHz and the resolution of 0.1. In fact, they cannot recognize the difference between duty cycles of 1.58 and 1.59 in 20 kHz. Therefore, in addition to the switching frequency f_{sw} and the resolution previously explained, there are many great constraints in their datasheets that must be compatible with the characteristics of the switches. Optocouplers are more expensive, but they provide isolation. To summarize, firstly, the IGBT gate driver must be fast enough that the switching frequency f_{sw} can easily be implemented. Secondly, the isolation exists between the control part and the power part. Thirdly, the resolution must be large enough to have accurate duty cycles.

3.7. Microcontroller

There are two crucial factors in the microcontroller selection:

- The clock of its central processing unit and its architecture.
  The clock of a microcontroller determines the speed of calculations. The microcontroller must be able to implement the control systems and its controllers as fast as possible. ARM Cortex-M (ARM LPC1768 as a case in point), STM32, and DSP C2000 (TMS320F28335 as a case in point) are well-known microcontrollers for implementing the control systems similar to what has been illustrated in Figure 4. The architecture of processors commonly falls into two groups: reduced-instruction-set computing (RISC) and complex-instruction-set computing (CISC). The microcontrollers with CISC architecture are better and faster than the ones with RISC architecture for implementing the control loops because they inherently have the discrete structures for filters and signal processing of the control systems. They perform the same calculations

faster (10 times faster or even more) in comparison with RISC microcontrollers for a specified clock frequency.

- The frequency of the analogue-to-digital converter, f_s.

  Nyquist theory states that a periodic signal must be sampled at more than twice the highest frequency component of the signal. In practice, it should be more than 10 times. Therefore, in order to recreate the current and voltages sensed for the control system, the analogue-to-digital converter must be as fast as possible. The accuracy of the analogue-to-digital converter is also an important factor. Thus, the designer should notice the conversion step.

3.8. Voltage and Current Sensors

There are two common methods for current measurement: hall-effect current sensors and a very precise power resistor, as shown in Figure 8 [57,58]. ACS712 05B is a hall-effect current sensor with a bandwidth of 80 kHz. This bandwidth can be modelled with a first-order transfer function [7]. This model has been shown in Figure 4 in the form of a block diagram. τ_f denotes the time constant of the first-order transfer function. According to linear control theories, the bandwidth of this transfer function equals $1/\tau_f$. Additionally, the current can be measured by another method. A very precise power resistor (0.1 Ω 10 W) along with an isolated difference amplifier, HCPL 7800, are used to measure the current. This method has higher speed and better bandwidth, but it costs more and is a little hard to implement. It also creates isolation between power and control parts due to the isolated difference amplifier. The outputs are analogue signals that are interpreted by the microcontroller. To protect the control system from transient and steady overvoltages, it can be equipped with the zener diodes, small-signal schottky diodes, and resettable fuses. The bandwidth of the sensors should be considered at least ten times greater than the highest frequency component of the current or voltage signal according to Nyquist theory about sampling. The switching frequency f_{sw} is the highest frequency component of these signals regardless of noises and distortions. Therefore, the bandwidths of the sensors are crucial factors for microcontrollers, as well as reliability of the control system. If the bandwidths of the sensors are small in comparison to the bandwidths of the closed loops, the reliability and stability in the control loops are also threatened. For higher frequencies and accuracies, very precise power resistors and isolated difference amplifiers such as HCPL 7800 are recommended. It is worth mentioning that Op Amps and isolation amplifiers can have greater bandwidths and accuracies in comparison with hall-effect current sensors. However, they increase the cost a little.

Figure 9 shows a common circuit for measuring the voltage in a converter. It senses the voltages with considerable bandwidth and accuracy. It includes very precise resistors in series. The voltage is measured by voltage division idea between the two resistances connected in series. Then, this combination is connected to the voltage that is supposed to be measured. The leakage current is negligible because the equivalent resistance is very high in the range of MΩ. The voltage difference across the lower resistance is given to an isolated difference amplifier, for instance, HCPL 7800. This method also creates isolation between power and control parts due to the isolated difference amplifier. It has good bandwidth (100 kHz), but it costs more and is a little hard to implement. The resistances should be selected as accurately as possible. Resistances with 0.5 percent or 0.1 percent accuracy are very expensive. The inputs of this board are the voltage terminals, and the outputs are analogue signals that are interpreted by the microcontroller. To protect the control system from transient and steady overvoltages, it can be equipped with the zener diodes, small-signal Schottky diodes, and resettable fuses.

Please refer to the main electronic elements in Figures 8 and 9 again. i_B is measured based on the previously mentioned methods. On the other hand, v_B and v_{DC} are measured by using HCPL 7800 and OP 37G. The circuit bandwidth depends on some factors. The speeds of the operational amplifiers, OP 37G, in the voltage and current sensing boards are very high. Since very accurate high-speed operational amplifiers have been selected,

the bandwidths of the voltage and current sensors (HCPL 7800 and ACS712 05B) determine the overall bandwidths. These bandwidths can be modelled by the block diagrams shown in Figure 4.
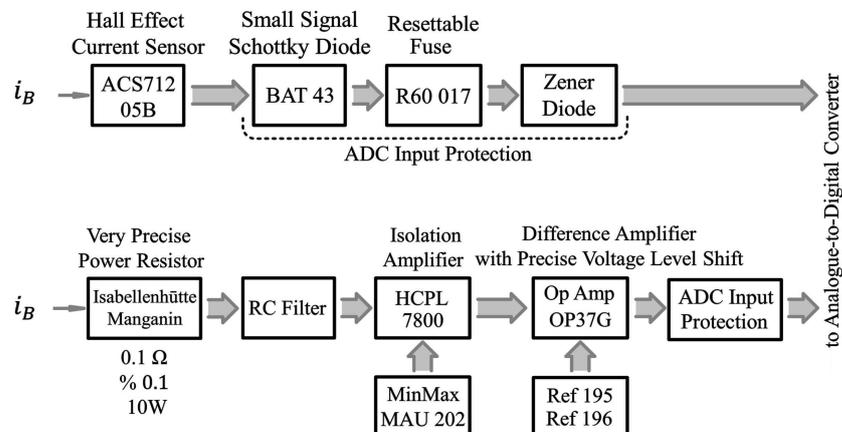

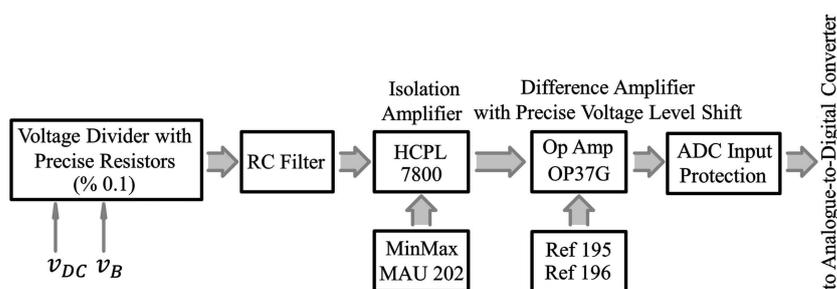**Figure 8.** Two common circuits to measure current in a converter.

Figure 9. A common circuit to measure voltage in a converter.

3.9. Maximum Level of Battery Current and Power

From the standpoint of electrical engineering, injecting current to and extracting current from a battery can result in charging and discharging, respectively (see Figure 10). According to the shape of this waveform, charging–discharging techniques fall into some of the following categories: constant current, constant voltage [59,60], sinusoidal-ripple current [3,61–64], pulse voltage [2,65–69], pulse current [1,6,10,19,70–73], and reflex [20,45,74–79]. Figure 10 summarizes the waveforms of these techniques. The waveforms, whether voltage or current, can be sinusoidal with a non-zero average, positive pulse, negative pulse, or constant. Depending on the adopted technique, the DC-DC stage and the IGBT leg in the DC-DC stage here, with the aid of its control system, must operate as a voltage source or a current source so as to impose the desired voltage or current waveform, respectively, on the battery pack. The design of the control system of the IGBT leg to behave similar to an independent voltage source as well as an independent current source has been explained in detail in [1–3,7].

A combination of these waveforms creates the charging–discharging algorithm. Thus, particular charging–discharging techniques and particular waveforms may be used in the algorithm. Depending on the chemistry of the battery pack, Li-ion or Ni-MH or something else for EVs [80], the charging–discharging techniques and algorithms are adopted. The former is performed by the IGBT leg with its control system, and the latter is implemented by the microcontroller. With respect to the charging–discharging algorithms, assume a constant-current constant-voltage (CC-CV) algorithm, which is very well-known among researchers [59]. In this algorithm, the battery management subsystem senses the terminal voltage of the battery at each moment. Then, it calculates and sends reference commands to the control system. It stops injecting constant-current waveform to the

battery and starts imposing constant-voltage waveform if the battery voltage exceeds its maximum permissible value. The tool to generate various voltage and current waveforms regardless of the algorithm has been shown in Figures 1–4. The algorithm is defined by designers and is embedded in the battery management subsystem. The waveforms are enforced by the IGBT leg system with its control system, and the algorithm is programmed in the microcontroller as the brain of the system. The microcontroller gives the reference commands directly to the control system. The algorithms are very important in the battery performance and can be passive or even active [59]. Figure 4 shows the control system which receives the reference commands for the battery current i_B^* and the battery voltage v_B^* and imposes them on the battery. Figures 1 and 2 show the general overview of these control loops.
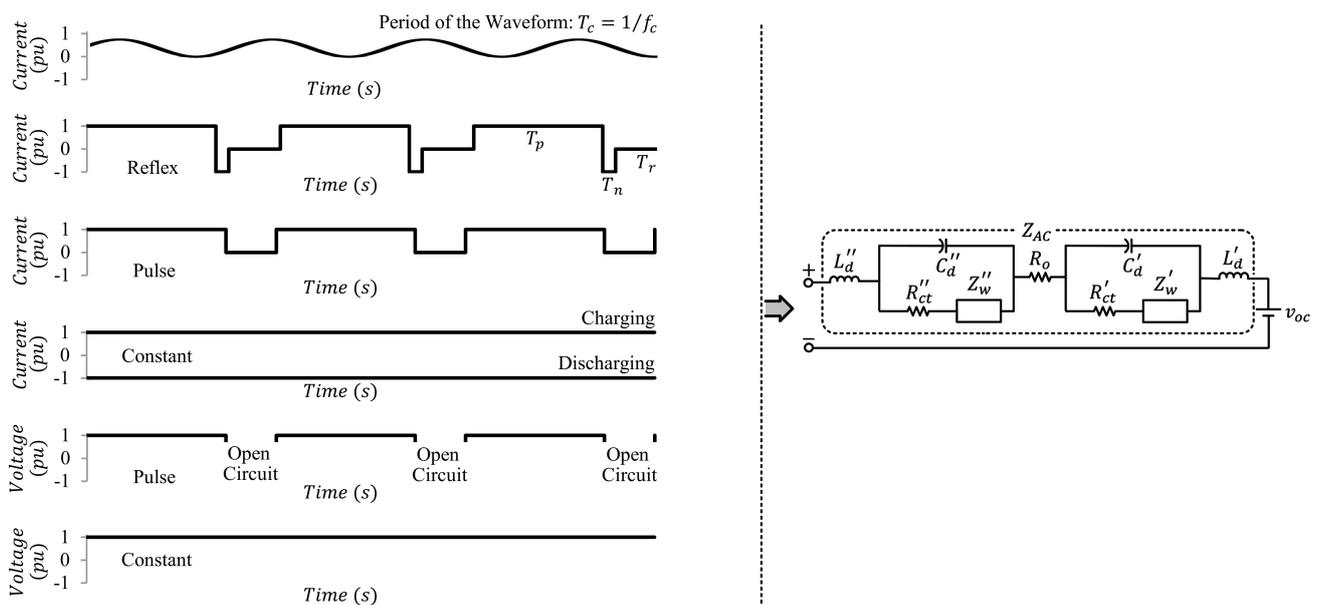

Figure 10. Various voltage and current waveforms for charging and discharging.

Battery models can be electrochemical, mathematical, and electrical [81,82]. The electrical models are made up of electrical components and are easier for electrical engineers to predict behaviour and parameters of the battery such as capacity, lifetime, state of charge (SOC), and so on [81,83]. Most of the electrical models can be classified into Thevenin-based [81], impedance-based [80–82,84–87], and runtime-based models [81]. They can describe the battery in the long term, the short term, and transients. Based on the impedance-based models, the online EIS has been developed as a strong analysis for calculating the parameters such as the state of health (SOH) and state of charge (SOC), which greatly represent the battery conditions. One group of the online EIS utilizes power electronic converters of the battery charger to generate battery voltage and current waveforms so as to estimate the battery parameters [88]. Interestingly, in [13,88–90], an IGBT leg is responsible for generating such waveforms.

Since the current and voltage waveforms shown in Figure 10 have short-term variations under one second, an AC impedance model is used for the battery in power electronic studies [3,61–63,81]. In [91], the behaviour of Li-ion batteries and unltracapacitors for EV power electronic applications is examined. In [92], some battery models are studied for various applications. The parameters in the AC impedance model illustrated in Figure 10 are changed by the temperature, state of charge (SOC), state of health (SOH), charging–discharging rates, and so forth [85]. Figure 11 shows how the real and imaginary parts of the AC impedance illustrated in Figure 10 vary according to temperature, state of charge (SOC), and state of health (SOH). The issues about the electrode, electrolyte, electrode/electrolyte interface, and ionic and electrical conductivity of the electrode in [93]

are considered as battery specifications and eventually determine the amplitude, frequency, and time intervals of the waveforms shown in Figure 10 as well as the charging–discharging algorithm executed in the microcontroller.
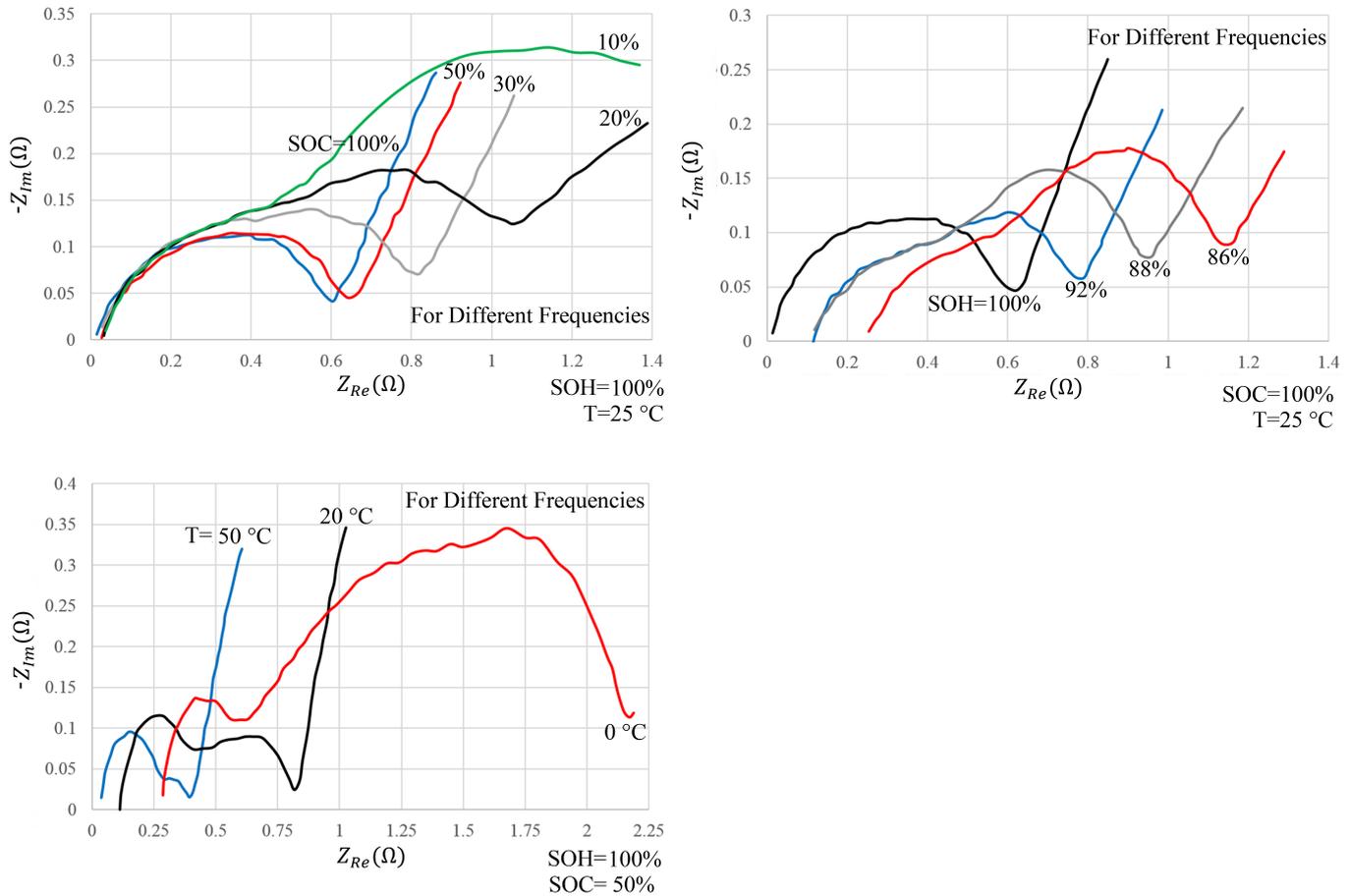

Figure 11. The effect of temperature (T), state of health (SOH), and state of charge (SOC) on the real and imaginary parts of the AC impedance of a Li-ion battery [85].

Assume that the battery is supposed to be charged, and i_B^* is being injected to the battery. The maximum battery current ($i_{B_{Max}}^*$) determines the the maximum power which can be injected to the battery. It equals $P_{B_{Max}} = i_{B_{Max}}^* \times v_B$. $P_{B_{Max}}$ means the maximum speed for charging or discharging. The maximum battery current ($i_{B_{Max}}^*$) is restricted by some factors:

- The voltage difference between v_{DC} and v_B;
  Reduction in v_{DC} is unfavourable because it may operate under the saturation situation. Moreover, v_{DC} would not be powerful enough in even duty cycles close to one to make the reference currents. The control loops approximate to the saturation condition. Moreover, a drop in v_{DC} decreases cost and the switching dissipation.
- The sum of (r_{on}) and (R) in each leg, and the equivalent resistance of each leg.
  The current delivered to the battery is the result of the voltage difference between v_{DC} and v_B over this resistance. Thus, better elements with lower resistances significantly enhance the ability of the system to deliver more power to the battery pack during charging or draw more power from the battery during discharging. Elements with lower resistances also decrease conduction losses according to (7).
- The ability of the elements to tolerate the current and voltage levels, for instance, diameters of the wires of the inductors.

3.10. Other Issues

The mentioned cases are not certainly the whole story. EV battery systems can also be viewed from various other perspectives, which have been ignored in this paper, such as the chemistry and characteristics of the battery pack, the elements of the battery cell [94,95], the materials used in the battery cell [94,95], the management of EV battery chargers throughout the microgrid [96], their efficiency and emissions [97], their role in ancillary services in vehicle-to-grid technology [98,99], and so forth.

4. Conclusions

Some important worthwhile experiences about design of EV battery chargers were presented. It addressed the efficiency, conduction losses, switching losses, switching frequency, sampling frequency, charging–discharging frequency, charging–discharging algorithm, voltage stress, switch gate drivers, isolation, selection of voltage and current levels, battery current ripple, bandwidths of the sensors and control loops, accuracy of the sensors and microcontroller, and maximum power of the battery charger. The stated technical considerations and the experiences are not limited to a particular topology and will definitely help engineers in carefully and cleverly designing EV battery chargers.

Author Contributions: Conceptualization, M.B.; methodology, M.B.; software, M.B. and M.F.; validation, M.B.; formal analysis, M.B. and M.F.; investigation, M.B.; writing—original draft preparation, G.B.G. and K.T.; writing—review and editing, M.A. and K.T.; supervision, G.B.G.; project administration, M.A.; All authors have read and agreed to the published version of the manuscript.

Conflicts of Interest: The authors declare no conflict of interest.

Abbreviations

The following abbreviations are used in this manuscript:

AC:	Alternating current;
EIS:	Electrochemical Impedance Spectroscopy;
DC:	Direct current;
EV:	Electric vehicle;
IC:	Integrated circuit;
IGBT:	Insulated-gate bipolar transistor;
PWM:	Pulse width modulation;
T_c:	Period of pulse-current waveform;
f_c:	Frequency of pulse-current waveform;
f_s:	Sampling frequency of analogue-to-digital converter;
f_{sw}:	Switching frequency in PWM;
T_{sw}:	Switching period in PWM;
v_B:	Terminal battery voltage;
v_{DC}:	DC link voltage;
C_{DC}:	DC link capacitor;
C':	Capacitor linked in parallel with the battery. It is connected if the voltage control system works;
i_B:	Current flowing through L_B;
$i_{B_{Max}}$:	Maximum battery current;
i_{ext}:	Current injected to C_{DC};

i'_{ext}:	Current injected to the battery;
L_B:	Inductor of the leg Q_7Q_8 connected to the battery;
L:	Inductor for the three-phase legs in the DC-AC stage converter;
P_B:	Power injected by the leg Q_7Q_8 to the battery. It equals $v_B i_B$;
$P_{B_{Max}}$:	Maximum battery power and maximum power of the battery charger;
P_{ext}:	Power injected to C_{DC} by both the legs Q_7Q_8. It equals $v_{DC}i_{ext}$;
P_s:	AC-side three-phase terminal active power;
Q_s:	AC-side three-phase terminal reactive power;
i_s:	AC-side terminal current;
v_s:	Line-line AC-side terminal voltage;
$\triangle^*$:	Reference command of the variable $\triangle$ which is defined by the designer;
$\triangle_{ref}$:	Reference of the variable $\triangle$ which is generated by the outer control loops;
d_B:	Duty cycle in PWM strategy for the leg Q_7Q_8 connected to the battery;
τ_f:	Time constant of the current sensor;
τ'_f:	Time constant of the voltage sensor;
Q_i:	Switch number i.

References

1. Bayati, M.; Abedi, M.; Farahmandrad, M.; Gharehpetian, G.B. Delivering Smooth Power to Pulse-Current Battery Chargers: Electric Vehicles as a Case in Point. *IEEE Trans. Power Electron.* **2020**, *36*, 1295–1302. [CrossRef]
2. Bayati, M.; Abedi, M.; Gharehpetian, G.B.; Farahmandrad, M. Two designs for DC–DC stage of electric vehicle charging stations. *Electr. Eng.* **2020**, *107*, 2411–2502. [CrossRef]
3. Bayati, M.; Abedi, M.; Gharehpetian, G.B.; Farahmandrad, M. Sinusoidal-Ripple Current Control in Battery Charger of Electric Vehicles. *IEEE Trans. Veh. Technol.* **2020**, *69*, 7201–7210. [CrossRef]
4. Bayati, M.; Abedi, M.; Gharehpetian, G.B.; Farahmandrad, M. Short-term interaction between electric vehicles and microgrid in decentralized vehicle-to-grid control methods. *Prot. Control Mod. Power Syst.* **2019**, *4*, 5. [CrossRef]
5. Bayati, M.; Salmani, A.; Abedi, M.; Gharepetian, G.B. Control of EV/PHEV bidirectional battery chargers in AC microgrids. In Proceedings of the 2015 International Conference on Power, Instrumentation, Control and Computing (PICC), Thrissur, India, 9–11 December 2015; pp. 1–6.
6. Bayati, M.; Abedi, M.; Gharehpetian, G.B. A new electric vehicle charging station based on pulse current charging method. In Proceedings of the 2017 Iranian Conference on Electrical Engineering (ICEE), Tehran, Iran, 2–4 May 2017; pp. 967–972.
7. Yazdani, A.; Iravani, R. *Voltage-Sourced Converters in Power Systems*; Wiley Online Library: Hoboken, NJ, USA, 2010; Volume 34.
8. Tabari, M.; Yazdani, A. Stability of a DC distribution system for power system integration of plug-in hybrid electric vehicles. *IEEE Trans. Smart Grid* **2014**, *5*, 2564–2573. [CrossRef]
9. Jiang, Z.; Dougal, R.A. Control strategies for active power sharing in a fuel-cell-powered battery-charging station. *IEEE Trans. Ind. Appl.* **2004**, *40*, 917–924. [CrossRef]
10. Jiang, Z.; Dougal, R.A. Synergetic control of power converters for pulse current charging of advanced batteries from a fuel cell power source. *IEEE Trans. Power Electron.* **2004**, *19*, 1140–1150. [CrossRef]
11. Liu, P.J.; Yen, C.H. A fast-charging switching-based charger with adaptive hybrid duty cycle control for multiple batteries. *IEEE Trans. Power Electron.* **2017**, *32*, 1975–1983. [CrossRef]
12. Wang, J.; Chuang, C. Design considerations of microprocessor-controlled multiphase battery charger with fast-charging strategy. *IET Electr. Power Appl.* **2007**, *1*, 143–152. [CrossRef]
13. Qahouq, J.A.A.; Xia, Z. Single-perturbation-cycle online battery impedance spectrum measurement method with closed-loop control of power converter. *IEEE Trans. Ind. Electron.* **2017**, *64*, 7019–7029. [CrossRef]
14. Khaligh, A.; Li, Z. Battery, ultracapacitor, fuel cell, and hybrid energy storage systems for electric, hybrid electric, fuel cell, and plug-in hybrid electric vehicles: State of the art. *IEEE Trans. Veh. Technol.* **2010**, *59*, 2806–2814. [CrossRef]
15. Cao, J.; Emadi, A. A new battery/ultracapacitor hybrid energy storage system for electric, hybrid, and plug-in hybrid electric vehicles. *IEEE Trans. Power Electron.* **2012**, *27*, 122–132.
16. Tehrani, K. A smart cyber physical multi-source energy system for an electric vehicle prototype. *J. Syst. Archit.* **2020**, *111*, 101804. [CrossRef]
17. Kesler, M.; Kisacikoglu, M.C.; Tolbert, L.M. Vehicle-to-grid reactive power operation using plug-in electric vehicle bidirectional offboard charger. *IEEE Trans. Ind. Electron.* **2014**, *61*, 6778–6784. [CrossRef]
18. Kisacikoglu, M.C.; Kesler, M.; Tolbert, L.M. Single-phase on-board bidirectional PEV charger for V2G reactive power operation. *IEEE Trans. Smart Grid* **2015**, *6*, 767–775. [CrossRef]
19. Chen, L.R.; Young, C.M.; Chu, N.Y.; Liu, C.S. Phase-locked bidirectional converter with pulse charge function for 42-V/14-V dual-voltage Power Net. *IEEE Trans. Ind. Electron.* **2011**, *58*, 2045–2048. [CrossRef]
20. Chen, L.R.; Chu, N.Y.; Wang, C.S.; Liang, R.H. Design of a Reflex-based bidirectional converter with the energy recovery function. *IEEE Trans. Ind. Electron.* **2008**, *55*, 3022–3029. [CrossRef]

21. Falahi, M.; Chou, H.M.; Ehsani, M.; Xie, L.; Butler-Purry, K.L. Potential power quality benefits of electric vehicles. *IEEE Trans. Sustain. Energy* **2013**, *4*, 1016–1023.

22. Gallardo-Lozano, J.; Milanés-Montero, M.I.; Guerrero-Martínez, M.A.; Romero-Cadaval, E. Electric vehicle battery charger for smart grids. *Electr. Power Syst. Res.* **2012**, *90*, 18–29. [CrossRef]

23. Haghbin, S.; Lundmark, S.; Alakula, M.; Carlson, O. Grid-connected integrated battery chargers in vehicle applications: Review and new solution. *IEEE Trans. Ind. Electron.* **2012**, *60*, 459–473. [CrossRef]

24. Hu, K.W.; Liaw, C.M. On a bidirectional adapter with G2B charging and B2X emergency discharging functions. *IEEE Trans. Ind. Electron.* **2013**, *61*, 243–257. [CrossRef]

25. Rivera, S.; Wu, B.; Kouro, S.; Yaramasu, V.; Wang, J. Electric vehicle charging station using a neutral point clamped converter with bipolar DC bus. *IEEE Trans. Ind. Electron.* **2014**, *62*, 1999–2009. [CrossRef]

26. Dusmez, S.; Khaligh, A. Generalized technique of compensating low-frequency component of load current with a parallel bidirectional DC/DC converter. *IEEE Trans. Power Electron.* **2014**, *29*, 5892–5904. [CrossRef]

27. Kollimalla, S.K.; Mishra, M.K.; Narasamma, N.L. Design and analysis of novel control strategy for battery and supercapacitor storage system. *IEEE Trans. Sustain. Energy* **2014**, *5*, 1137–1144. [CrossRef]

28. Khan, S.A.; Islam, M.R.; Guo, Y.; Zhu, J. A new isolated multi-port converter with multi-directional power flow capabilities for smart electric vehicle charging stations. *IEEE Trans. Appl. Supercond.* **2019**, *29*, 1–4. [CrossRef]

29. Hu, Y.; Gan, C.; Hu, S.; Cao, W.; Wang, X.; Finney, S. Winding-centre-tapped switched reluctance motor drive for multi-source charging in electric vehicle applications. *IET Power Electron.* **2015**, *8*, 2067–2075. [CrossRef]

30. Szymanski, J.R.; Zurek-Mortka, M.; Wojciechowski, D.; Poliakov, N. Unidirectional DC/DC converter with voltage inverter for fast charging of electric vehicle batteries. *Energies* **2020**, *13*, 4791. [CrossRef]

31. Bassa de los Mozos, A.; Chandra Mouli, G.R.; Bauer, P. Evaluation of topologies for a solar powered bidirectional electric vehicle charger. *IET Power Electron.* **2019**, *12*, 3675–3687. [CrossRef]

32. Monteiro, V.; Ferreira, J.C.; Melendez, A.A.N.; Couto, C.; Afonso, J.L. Experimental validation of a novel architecture based on a dual-stage converter for off-board fast battery chargers of electric vehicles. *IEEE Trans. Veh. Technol.* **2017**, *67*, 1000–1011. [CrossRef]

33. Sayed, K.; Gabbar, H.A. Electric vehicle to power grid integration using three-phase three-level AC/DC converter and PI-fuzzy controller. *Energies* **2016**, *9*, 532. [CrossRef]

34. Kumar, G.G.; Sundaramoorthy, K.; Athikkal, S.; Karthikeyan, V. Dual input superboost DC–DC converter for solar powered electric vehicle. *IET Power Electron.* **2019**, *12*, 2276–2284. [CrossRef]

35. Chauhan, S.; Singh, B. Grid-interfaced solar PV powered electric vehicle battery system with novel adaptive digital control algorithm. *IET Power Electron.* **2019**, *12*, 3470–3478. [CrossRef]

36. Li, M.; Xu, H.; Li, W.; Liu, Y.; Li, F.; Hu, Y.; Liu, L. The structure and control method of hybrid power source for electric vehicle. *Energy* **2016**, *112*, 1273–1285. [CrossRef]

37. Liu, S.; Xie, X.; Yang, L. Analysis, modeling and implementation of a switching bi-directional buck-boost converter based on electric vehicle hybrid energy storage for V2G system. *IEEE Access* **2020**, *8*, 65868–65879. [CrossRef]

38. Khan, M.S.; Ahmad, I.; Abideen, F.Z.U. Output voltage regulation of FC-UC based hybrid electric vehicle using integral backstepping control. *IEEE Access* **2019**, *7*, 65693–65702. [CrossRef]

39. Araria, R.; Berkani, A.; Negadi, K.; Marignetti, F.; Boudiaf, M. Performance analysis of DC-DC converter and DTC based fuzzy logic control for power management in electric vehicle application. *J. Eur. Des Syst. Autom.* **2020**, *53*, 1–9. [CrossRef]

40. Atawi, I.E.; Hendawi, E.; Zaid, S.A. Analysis and Design of a Standalone Electric Vehicle Charging Station Supplied by Photovoltaic Energy. *Processes* **2021**, *9*, 1246. [CrossRef]

41. Mesbahi, T.; Rizoug, N.; Khenfri, F.; Bartholomeüs, P.; Le Moigne, P. Dynamical modelling and emulation of Li-ion batteries–supercapacitors hybrid power supply for electric vehicle applications. *IET Electr. Syst. Transp.* **2017**, *7*, 161–169. [CrossRef]

42. Sellali, M.; Abdeddaim, S.; Betka, A.; Djerdir, A.; Drid, S.; Tiar, M. Fuzzy-super twisting control implementation of battery/super capacitor for electric vehicles. *ISA Trans.* **2019**, *95*, 243–253. [CrossRef]

43. Monteiro, V.; Pinto, J.; Afonso, J.L. Operation modes for the electric vehicle in smart grids and smart homes: Present and proposed modes. *IEEE Trans. Veh. Technol.* **2015**, *65*, 1007–1020. [CrossRef]

44. Marra, F.; Yang, G.Y.; Træholt, C.; Larsen, E.; Østergaard, J.; Blažič, B.; Deprez, W. EV charging facilities and their application in LV feeders with photovoltaics. *IEEE Trans. Smart Grid* **2013**, *4*, 1533–1540. [CrossRef]

45. Bayati, M.; Abedi, M.; Hosseinian, H.; Gharehpetian, G.B. A novel control strategy for Reflex-based electric vehicle charging station with grid support functionality. *J. Energy Storage* **2017**, *12*, 108–120. [CrossRef]

46. Yilmaz, M.; Krein, P.T. Review of battery charger topologies, charging power levels, and infrastructure for plug-in electric and hybrid vehicles. *IEEE Trans. Power Electron.* **2013**, *28*, 2151–2169. [CrossRef]

47. Hajiaghasi, S.; Salemnia, A.; Hamzeh, M. Hybrid energy storage system for microgrids applications: A review. *J. Energy Storage* **2019**, *21*, 543–570. [CrossRef]

48. Savio, D.A.; Juliet, V.A.; Chokkalingam, B.; Padmanaban, S.; Holm-Nielsen, J.B.; Blaabjerg, F. Photovoltaic integrated hybrid microgrid structured electric vehicle charging station and its energy management approach. *Energies* **2019**, *12*, 168. [CrossRef]

49. Oh, C.Y.; Kim, D.H.; Woo, D.G.; Sung, W.Y.; Kim, Y.S.; Lee, B.K. A high-efficient nonisolated single-stage on-board battery charger for electric vehicles. *IEEE Trans. Power Electron.* **2013**, *28*, 5746–5757. [CrossRef]

50. *Electric Vehicle and Plug in Hybrid Electric Vehicle Conductive Charge Coupler*; SAE Recommended Practice: Warrendale, PA, USA, 2010.

51. Habib, S.; Khan, M.M.; Abbas, F.; Sang, L.; Shahid, M.U.; Tang, H. A comprehensive study of implemented international standards, technical challenges, impacts and prospects for electric vehicles. *IEEE Access* **2018**, *6*, 13866–13890. [CrossRef]

52. Kim, S.Y.; Song, H.S.; Nam, K. Idling port isolation control of three-port bidirectional converter for EVs. *IEEE Trans. Power Electron.* **2012**, *27*, 2495–2506. [CrossRef]

53. De Breucker, S.; Engelen, K.; D'hulst, R.; Driesen, J. Impact of current ripple on Li-ion battery ageing. *World Electr. Veh. J.* **2013**, *6*, 532–540. [CrossRef]

54. Bessman, A.; Soares, R.; Wallmark, O.; Svens, P.; Lindbergh, G. Aging effects of AC harmonics on lithium-ion cells. *J. Energy Storage* **2019**, *21*, 741–749. [CrossRef]

55. Korth Pereira Ferraz, P.; Kowal, J. A Comparative Study on the Influence of DC/DC-Converter Induced High Frequency Current Ripple on Lithium-Ion Batteries. *Sustainability* **2019**, *11*, 6050. [CrossRef]

56. Semiconductors, V. IGBT/MOSFET Gate Drive Optocoupler. *Retrieved* **2011**, *26*, 2007–2008.

57. Patel, A.; Ferdowsi, M. Current sensing for automotive electronics—A survey. *IEEE Trans. Veh. Technol.* **2009**, *58*, 4108–4119. [CrossRef]

58. Ziegler, S.; Woodward, R.C.; Iu, H.H.C.; Borle, L.J. Current sensing techniques: A review. *IEEE Sens. J.* **2009**, *9*, 354–376. [CrossRef]

59. Gao, Y.; Zhang, X.; Cheng, Q.; Guo, B.; Yang, J. Classification and review of the charging strategies for commercial lithium-ion batteries. *IEEE Access* **2019**, *7*, 43511–43524. [CrossRef]

60. Hussein, A.A.H.; Batarseh, I. A review of charging algorithms for nickel and lithium battery chargers. *IEEE Trans. Veh. Technol.* **2011**, *60*, 830–838. [CrossRef]

61. Chen, L.R.; Wu, S.L.; Shieh, D.T.; Chen, T.R. Sinusoidal-ripple-current charging strategy and optimal charging frequency study for Li-ion batteries. *IEEE Trans. Ind. Electron.* **2013**, *60*, 88–97. [CrossRef]

62. Chen, L.R.; Chen, J.J.; Ho, C.M.; Wu, S.L.; Shieh, D.T. Improvement of Li-ion battery discharging performance by pulse and sinusoidal current strategies. *IEEE Trans. Ind. Electron.* **2013**, *60*, 5620–5628. [CrossRef]

63. Cho, S.Y.; Lee, I.O.; Baek, J.I.; Moon, G.W. Battery impedance analysis considering DC component in sinusoidal ripple-current charging. *IEEE Trans. Ind. Electron.* **2015**, *63*, 1561–1573. [CrossRef]

64. Bessman, A.; Soares, R.; Vadivelu, S.; Wallmark, O.; Svens, P.; Ekström, H.; Lindbergh, G. Challenging sinusoidal ripple-current charging of lithium-ion batteries. *IEEE Trans. Ind. Electron.* **2017**, *65*, 4750–4757. [CrossRef]

65. Chen, L.R. Design of duty-varied voltage pulse charger for improving Li-ion battery-charging response. *IEEE Trans. Ind. Electron.* **2009**, *56*, 480–487. [CrossRef]

66. Chen, L.R. A design of an optimal battery pulse charge system by frequency-varied technique. *IEEE Trans. Ind. Electron.* **2007**, *54*, 398–405. [CrossRef]

67. Yin, M.; Cho, J.; Park, D. Pulse-based fast battery IoT charger using dynamic frequency and duty control techniques based on multi-sensing of polarization curve. *Energies* **2016**, *9*, 209. [CrossRef]

68. Amanor-Boadu, J.M.; Abouzied, M.A.; Sánchez-Sinencio, E. An efficient and fast Li-ion battery charging system using energy harvesting or conventional sources. *IEEE Trans. Ind. Electron.* **2018**, *65*, 7383–7394. [CrossRef]

69. Amanor-Boadu, J.M.; Guiseppi-Elie, A.; Sánchez-Sinencio, E. Search for optimal pulse charging parameters for Li-Ion polymer batteries using Taguchi orthogonal arrays. *IEEE Trans. Ind. Electron.* **2018**, *65*, 8982–8992. [CrossRef]

70. Amanor-Boadu, J.; Guiseppi-Elie, A.; Sánchez-Sinencio, E. The Impact of Pulse Charging Parameters on the Life Cycle of Lithium-ion Polymer Batteries. *Energies* **2018**, *11*, 2162. [CrossRef]

71. Chen, L.R.; Chen, J.J.; Chu, N.Y.; Han, G.Y. Current-pumped battery charger. *IEEE Trans. Ind. Electron.* **2008**, *55*, 2482–2488. [CrossRef]

72. Purushothaman, B.; Landau, U. Rapid charging of lithium-ion batteries using pulsed currents a theoretical analysis. *J. Electrochem. Soc.* **2006**, *153*, A533–A542. [CrossRef]

73. Abdel-Monem, M.; Trad, K.; Omar, N.; Hegazy, O.; Van den Bossche, P.; Van Mierlo, J. Influence analysis of static and dynamic fast-charging current profiles on ageing performance of commercial lithium-ion batteries. *Energy* **2017**, *120*, 179–191. [CrossRef]

74. Chiu, H.J.; Lin, L.W.; Pan, P.L.; Tseng, M.H. A novel rapid charger for lead-acid batteries with energy recovery. *IEEE Trans. Power Electron.* **2006**, *21*, 640–647. [CrossRef]

75. Tsai, C.T.; Kuo, Y.C.; Kuo, Y.P.; Hsieh, C.T. A Reflex Charger with ZVS and Non-Dissipative Cells for Photovoltaic Energy Conversion. *Energies* **2015**, *8*, 1373–1389. [CrossRef]

76. Yong, J.Y.; Ramachandaramurthy, V.K.; Tan, K.M.; Mithulananthan, N. A review on the state-of-the-art technologies of electric vehicle, its impacts and prospects. *Renew. Sustain. Energy Rev.* **2015**, *49*, 365–385. [CrossRef]

77. Li, J.; Murphy, E.; Winnick, J.; Kohl, P.A. The effects of pulse charging on cycling characteristics of commercial lithium-ion batteries. *J. Power Sources* **2001**, *102*, 302–309. [CrossRef]

78. Monem, M.A.; Trad, K.; Omar, N.; Hegazy, O.; Mantels, B.; Mulder, G.; Van den Bossche, P.; Van Mierlo, J. Lithium-ion batteries: Evaluation study of different charging methodologies based on aging process. *Appl. Energy* **2015**, *152*, 143–155. [CrossRef]

79. Hsieh, H.I.; Tsai, C.Y.; Hsieh, G.C. Photovoltaic burp charge system on energy-saving configuration by smart charge management. *IEEE Trans. Power Electron.* **2014**, *29*, 1777–1790. [CrossRef]

80. Saldaña, G.; San Martín, J.I.; Zamora, I.; Asensio, F.J.; Oñederra, O. Analysis of the current electric battery models for electric vehicle simulation. *Energies* **2019**, *12*, 2750. [CrossRef]

81. Chen, M.; Rincón-Mora, G. Accurate electrical battery model capable of predicting runtime and IV performance. *Energy Convers. IEEE Trans.* **2006**, *21*, 504–511. [CrossRef]

82. Thiruvonasundari, D.; Deepa, K. Electric vehicle battery modelling methods based on state of charge—Review. *J. Green Eng.* **2020**, *10*, 24–61.

83. Ali, M.U.; Zafar, A.; Nengroo, S.H.; Hussain, S.; Junaid Alvi, M.; Kim, H.J. Towards a smarter battery management system for electric vehicle applications: A critical review of lithium-ion battery state of charge estimation. *Energies* **2019**, *12*, 446. [CrossRef]

84. Varnosfaderani, M.A.; Strickland, D. Online impedance spectroscopy estimation of a battery. In Proceedings of the 2016 18th European Conference on Power Electronics and Applications (EPE'16 ECCE Europe), Karlsruhe, Germany, 5–9 September 2016, pp. 1–10.

85. Westerhoff, U.; Kurbach, K.; Lienesch, F.; Kurrat, M. Analysis of lithium-ion battery models based on electrochemical impedance spectroscopy. *Energy Technol.* **2016**, *4*, 1620–1630. [CrossRef]

86. Wang, X.; Wei, X.; Zhu, J.; Dai, H.; Zheng, Y.; Xu, X.; Chen, Q. A review of modeling, acquisition, and application of lithium-ion battery impedance for onboard battery management. *ETransportation* **2020**, *7*, 100093. [CrossRef]

87. Stroe, D.I.; Swierczynski, M.; Stroe, A.I.; Kaer, S.K.; Teodorescu, R. Lithium-ion battery power degradation modelling by electrochemical impedance spectroscopy. *IET Renew. Power Gener.* **2017**, *11*, 1136–1141. [CrossRef]

88. Varnosfaderani, M.A.; Strickland, D. A Comparison of Online Electrochemical Spectroscopy Impedance Estimation of Batteries. *IEEE Access* **2018**, *6*, 23668–23677. [CrossRef]

89. Huang, W.; Qahouq, J.A.A. An online battery impedance measurement method using DC-DC power converter control. *IEEE Trans. Ind. Electron.* **2014**, *61*, 5987–5995. [CrossRef]

90. Lee, Y.D.; Park, S.Y.; Han, S.B. Online embedded impedance measurement using high-power battery charger. *IEEE Trans. Ind. Appl.* **2015**, *51*, 498–508. [CrossRef]

91. Buller, S.; Thele, M.; De Doncker, R.W.; Karden, E. Impedance-based simulation models of supercapacitors and Li-ion batteries for power electronic applications. *IEEE Trans. Ind. Appl.* **2005**, *41*, 742–747. [CrossRef]

92. Nikdel, M. Various battery models for various simulation studies and applications. *Renew. Sustain. Energy Rev.* **2014**, *32*, 477–485.

93. Zhu, G.L.; Zhao, C.Z.; Huang, J.Q.; He, C.; Zhang, J.; Chen, S.; Xu, L.; Yuan, H.; Zhang, Q. Fast Charging Lithium Batteries: Recent Progress and Future Prospects. *Small* **2019**, *15*, 1805389. [CrossRef]

94. Pan, H.; Huang, X.; Wang, C.; Liu, D.; Wang, D.; Zhang, R.; Li, S.; Lv, C.; Zhao, L.; Wang, J.; et al. Sandwich structural TixOy-Ti3C2/C3N4 material for long life and fast kinetics Lithium-Sulfur Battery: Bidirectional adsorption promoting lithium polysulfide conversion. *Chem. Eng. J.* **2021**, *410*, 128424. [CrossRef]

95. Rehman, S.; Khan, K.; Zhao, Y.; Hou, Y. Nanostructured cathode materials for lithium–sulfur batteries: progress, challenges and perspectives. *J. Mater. Chem. A* **2017**, *5*, 3014–3038. [CrossRef]

96. Singh, M.; Kumar, P.; Kar, I. Implementation of vehicle to grid infrastructure using fuzzy logic controller. *IEEE Trans. Smart Grid* **2012**, *3*, 565–577. [CrossRef]

97. Mehmood, K.; Iftikhar, Y.; Chen, S.; Amin, S.; Manzoor, A.; Pan, J. Analysis of Inter-Temporal Change in the Energy and CO_2 Emissions Efficiency of Economies: A Two Divisional Network DEA Approach. *Energies* **2020**, *13*, 3300. [CrossRef]

98. Yilmaz, M.; Krein, P.T. Review of the impact of vehicle-to-grid technologies on distribution systems and utility interfaces. *IEEE Trans. Power Electron.* **2012**, *28*, 5673–5689. [CrossRef]

99. Su, W.; Eichi, H.; Zeng, W.; Chow, M.Y. A survey on the electrification of transportation in a smart grid environment. *IEEE Trans. Ind. Inform.* **2011**, *8*, 1–10. [CrossRef]